Thermally Stable Transparent Resistive Random Access Memory based on All-Oxide Heterostructures

Jie Shang, Gang Liu, Huali Yang, Xiaojian Zhu, Xinxin Chen, Hongwei Tan, Benlin Hu, Liang Pan, Wuhong Xue, and Run-Wei Li**

An all-oxide transparent resistive random access memory (T-RRAM) device based on hafnium oxide (HfO_x) storage layer and indium-tin oxide (ITO) electrodes is fabricated in this work. The memory device demonstrates not only good optical transmittance but also a forming-free bipolar resistive switching behavior with room-temperature R_{OFF}/R_{ON} ratio of 45, excellent endurance of ≈5×10^7 cycles and long retention time over 10^6 s. More importantly, the HfO_x based RRAM carries great ability of anti-thermal shock over a wide temperature range of 10 K to 490 K, and the high R_{OFF}/R_{ON} ratio of ≈40 can be well maintained under extreme working conditions. The field-induced electrochemical formation and rupture of the robust metal-rich conductive filaments in the mixed-structure hafnium oxide film are found to be responsible for the excellent resistance switching of the T-RRAM devices. The present all-oxide devices are of great potential for future thermally stable transparent electronic applications.

1. Introduction

With its great potential to make significant impact in a wide variety of areas ranging from consumer products to industrial equipments, transparent electronics have been considered as an emerging technology for the next generation electronic circuitry and optoelectronic devices.[1] Transparent resistive random access memories (T-RRAMs), carrying the advantages of both invisible electronics[2] and RRAMs,[3] have also attracted tremendous amount of attention from both academic and industrial communities in recent years.[4] For instance, an all-transparent electronic gadget assembled with invisible memory, CPU, circuitry and display panel may receive good market response for better-life, while the transparent information storage device that is insensitive to the solar irradiation or demonstrates good thermal stability is of great importance for use under severe environmental conditions.[5]

To construct high-performance T-RRAMs, wide band-gap materials which are concurrently electrically-switchable and optically-transparent are necessary.[6] With this concern, opaque silicon-based semiconductors are no longer qualified, whereas metal oxides provide an alternative opportunity for discovering novel invisible electronic applications,[7] due to their distinctive magnetic and electronic properties arising from the diverse crystal structures and component elements. Previous efforts to produce T-RRAM generally focused on investigating the resistive switching properties of gadolinium oxide,[4a] titanium oxide,[4b] zinc oxide,[4c,d] and doped-zinc oxide[4e,f] thin films that are sandwiched between transparent conductive oxide (TCO) electrodes. With the wide band-gap of ≈ 5.40 eV, Gd_2O_3 exhibits a wide optical-window crossing the deep-ultraviolet to visible region.[4a] However, its resistive switching properties (set/reset voltages in particular) fluctuate seriously in a limited numbers of operating cycles. On the other hand, titanium oxide and (doped) zinc oxide exhibit better electrical behavior, but their relatively narrower band-gap (E_g ≈ 3.20 and 3.37 eV, respectively) inevitably shrinks the transparent width of the optical-window.[4b–f] Therefore, to receive both high optical transparency and good electronic performance in resistive switching metal oxides is still a pending challenge at the moment.[8] Nevertheless, the missing fundamental understanding of the resistive switching mechanism is the other obstacle that hinders the precise prediction of T-RRAM performance and further improvement of high-quality metal oxides.[9]

Hafnium oxide (HfO_x) is an inert, insulating and colorless material with a dielectric constant of around 25 and a band-gap of approximately 6 eV.[10,11] The high-κ nature of hafnium oxide makes it a leading candidate to replace silicon oxide gate insulator in field-effect transistors or charge-storage dielectric in DRAM capacitors,[12] while the wide band-gap offers an optical-window opening over the entire IR (≈10 μm) to deep-UV

Dr. J. Shang, Prof. G. Liu, H. L. Yang, X. J. Zhu, X. X. Chen, H. W. Tan, Dr. B. L. Hu, L. Pan, W. H. Xue, Prof. R.-W. Li
CAS Key Laboratory of Magnetic Materials and Devices
Ningbo Institute of Materials Technology and Engineering
Chinese Academy of Sciences
Ningbo, 315201, P. R. China
E-mail: liug@nimte.ac.cn; runweili@nimte.ac.cn
Dr. J. Shang, Prof. G. Liu, H. L. Yang, X. J. Zhu, X. X. Chen, H. W. Tan, Dr. B. L. Hu, L. Pan, W. H. Xue, Prof. R.-W. Li
Zhejiang Province Key Laboratory of Magnetic Materials and Application Technology
Ningbo Institute of Materials Technology and Engineering
Chinese Academy of Sciences
Ningbo, 315201, P. R. China

DOI: 10.1002/adfm.201303274

(≈200 nm) solar irradiation spectrum.[13] By incorporating high-κ amorphous hafnium oxide insulator into CMOS-compatible RRAMs, the current leakage issue can be effectively counteracted by eliminating/reducing leaking paths associated with the grain boundaries of polycrystalline films.[14] Consequently, the storage layer can be made even thinner to enhance both function density and optical transparency without sacrificing the device performance. With its melting point approaching 2800 °C, hafnium oxide will also be highly reliable against thermal shock when used in specific occasions.[15] Nevertheless, less effort has been devoted to explore the transparent and thermally stable application of hafnium oxide based resistive random access memories.

In this contribution, we report an all-oxide RRAM device based on indium-tin oxide/hafnium oxide/indium-tin oxide (ITO/HfO_x/ITO) sandwich structures. The ITO/HfO_x/ITO structure exhibits good optical-transparency of ≈80% in the visible region, which can be further enhanced over the deep-UV to IR solar spectrum by using the free-standing hafnium oxide film or employing more transparent electrodes. The all-oxide device demonstrates stable resistive switching behaviors, where the small set/reset voltages and moderate ON/OFF ratio are distributed uniformly for over 5×10^7 consecutive switching cycles or retained for 10^6 s. More importantly, the memory devices are resistant to violent thermal shock over a wide temperature range of 10 K to 490 K, demonstrating great potential for outer-space application under extreme working conductions. Elucidated by investigating the migration of oxygen ions and mapping the distribution of the electrochemically-reduced hafnium (Hf^0/Hf^{n+}, $0 < n < 4$) species via X-ray photoelectron spectroscopic analysis, the electric field-induced smooth formation and rupture of metal-rich conductive filaments through the mixed-structure hafnium oxide ultrathin film are found to be responsible for the stable switching of resistance of the all-oxide memory devices.

2. Results and Discussion

The resistive random access memory devices usually require a significant conductivity difference between the high resistance state (HRS) and low resistance state (LRS) for obtaining a large signal-to-noise ratio and lowering the possible misreading rate. For practical applications, the device needs to have high speed, low operating voltage, high endurance, long retention time and good switching reliability. To make it optically transparent, the storage layer should also be as thin as possible and maintain its electrical performance in the meanwhile. Therefore, it is essential to produce a high quality oxide film with excellent optical and electrical properties for the realization of T-RRAMs. The as-sputtered hafnium oxide layer, sandwiched between ITO/glass substrate and the top ITO electrode, was first visualized through a transmission electronic microscope (TEM) (**Figure 1**a). In obvious constrast to the brighter interfacial regions and the ITO layers, the darker hafnium oxide film shows a thickness of around 5 nm. AFM image also suggests the smooth nature of the HfO_x layer, which has a root-mean-square roughness (RMS) of less than 0.3 nm (Figure S1, Supporting Information).

The normal X-ray diffractive (XRD) pattern of the ITO-coated glass substrate and the polycrystalline HfO_x target, as well as the glazing-incidence X-ray diffractive (GIXRD) pattern of the 5 or 50 nm-HfO_x layers deposited on the ITO-coated glass substrates, are shown in Figure 1b, respectively. As expected, the ITO substrate exhibits XRD peaks at 21.5°, 30.0°, 35.2°, 37.3°, 45.2°, 50.4°, and 60.0°, respectively, which are corresponding to the <211>, <222>, <400>, <411>, <431>, <440>, and <622> planes of the polycrystalline indium-tin oxide. To examine the microstructure of the sputtering-deposited ultrathin hafnium oxide film, grazing-incidence X-ray diffraction (GIXRD) technique was employed instead with an X-ray beam incidence angle of 1° and a scanning step of 0.05° to eliminate the influence of the ITO substrate. However, the diffractive signal of the 5 nm-hafnium oxide layer is still too weak to be observed, and the 5 nm-HfO_x/ITO structure shows an XRD pattern that is almost identical to that of the ITO substrate. Further increase in the film thickness alters the XRD pattern significantly, and the 50 nm-HfO_x/ITO structure exhibits a wide and moderate GIXRD band covering the 26° to 30° range, indicating that both the amorphous and polycrystalline phases are present in the thicker film. By using the same deposition method and conditions, the 5 nm HfO_x film should also contain the mixed-crystalline structure as that of the thicker film. Nevertheless, TEM image indicates that the mixed-crystalline structure is composed of a polycrystalline HfO_x layer sandwiched between two amorphous interfacial layers. The presence of the amorphous regoins may act as protecting layers to screen the high leaking current along the large numbers of grain bournaries of the middle polycrystalline HfO_x thin film. In addition, according to the Schuller formula,[16]

$$d = \lambda / 2[\sin\theta_{n+1} - \sin\theta_n] \quad (1)$$

where d is the film thickness, λ is the wavelength of the X-ray beam, θ_{n+1} and θ_n are the reflective angle of the neighboring maximum of the reflected X-ray beam, the thickness of the ultrathin HfO_x layer is derived to be about 5 nm from the X-ray reflectivity (XRR) curve of Figure S2 (Supporting Information), which well agrees with that observed by TEM analysis.

Such a 5 nm-hafnium oxide film exerts little influence on the optical performance of the transparent conductive oxide (TCO) electrodes, and the ITO/HfO_x/ITO structured device demonstrate a good visible transmittance of ≈75% to 88% in the 400 nm to 800 nm region (Figure 1c,d). Further broadening of the optical window to the near infrared (IR)-visible (Vis)-deep ultraviolet (UV) region (2000 nm to 200 nm) leads to a notable decrease in the optical transmittance, which is attributed to the strong absorption of the ITO layer in the shorter-wavelength range.[17] Once the optical response of the ITO layer is deducted from the transmittance spectrum of the 5 nm-HfO_x/ITO structure, the ultrathin hafnium oxide film exhibits an almost complete transparency (>99%) over the entire UV-Vis-IR spectrum of the solar irradiation. The promising optical transparency, together with the ultrathin, ultra-smooth and mixed-structure nature of the hafnium oxide film, renders the all-oxide device promising memory capability and optical transmittance for T-RRAM applications.

The memory behavior of the transparent ITO/HfO_x/ITO structure is demonstrated by the current–voltage (I–V)

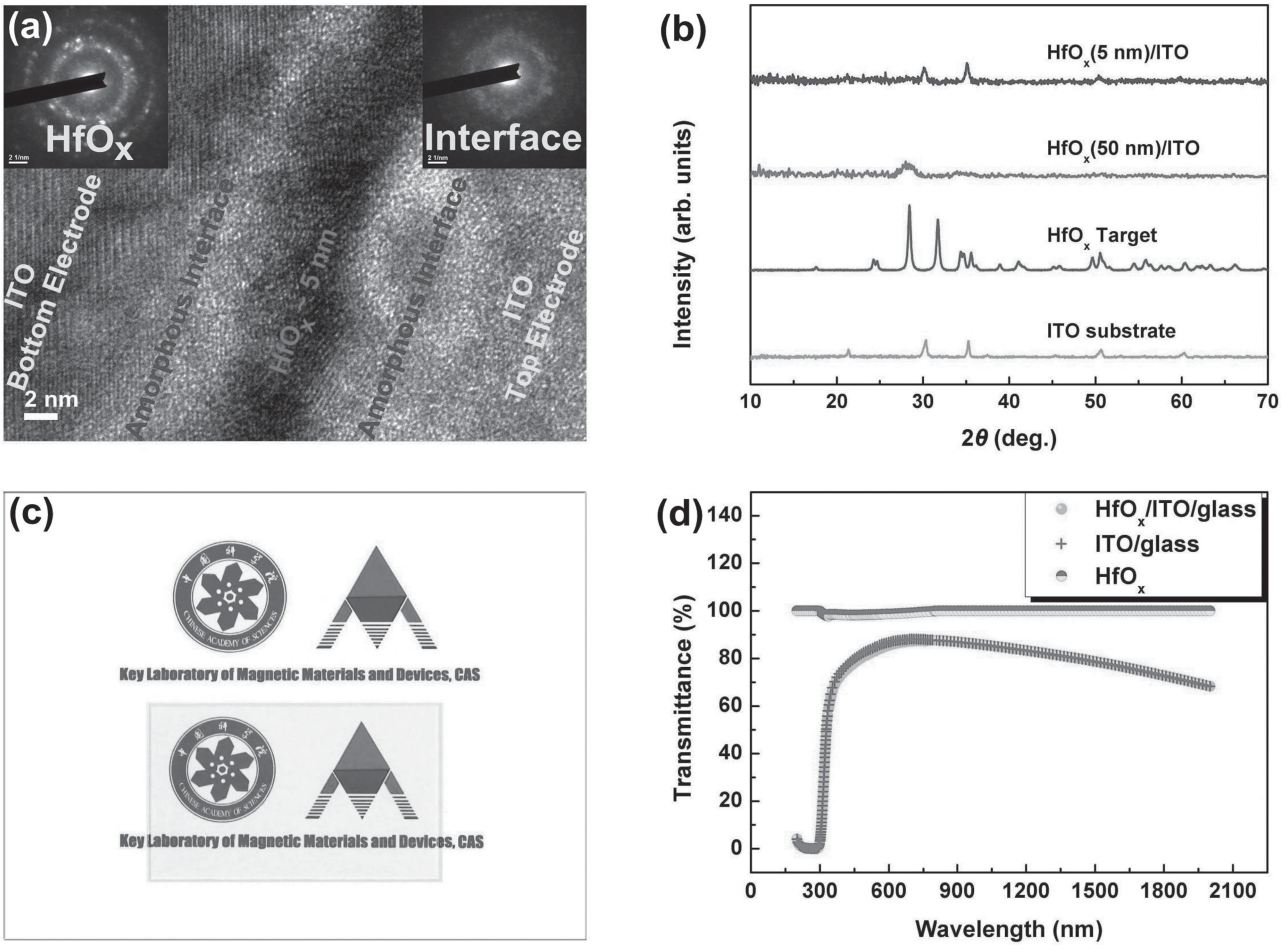

Figure 1. a) Transmission electron microscopic (TEM) cross-sectional view of the ITO/HfO_x/ITO structure. b) Glazing-incidence X-ray diffractive (GIXRD) pattern of the 5 or 50 nm -HfO_x layers deposited on the ITO-coated glass substrates, and normal X-ray diffractive (XRD) pattern of the poly-crystalline HfO_x target and the ITO-coated glass substrate, respectively. c) An ITO/HfO_x/ITO/glass structured sample device placed on top of the logo of Key Laboratory of Magnetic Materials and Devices, CAS (Chinese Academy of Sciences). d) Optical transmittance spectra of the ITO-coated glass substrate, ITO/HfO_x /ITO/glass sandwiched structure and the background- deducted ultrathin HfO_x layer.

characteristics (**Figure 2**a), which reveals a forming-free, bipolar and stable resistive switching effect under room temperature. Starting with the high resistance state (HRS or OFF state with an initial resistance of ≈1700 Ω read at –0.1 V) in the as-fabricated all-oxide cell, the current increases slowly with the increase in the applied positively-biased voltage. Without a forming process that requires a large setting voltage to initialize the switching of resistance as for other metal oxide based RRAMs,[4] the current flowing through the hafnium oxide layer increases abruptly from 1 mA to 20 mA at the small threshold voltage of 0.5 V, and switches the device (write or SET process) from the high resistance (OFF) state to the low resistance state (LRS or ON state). The low resistance state can be read in the following positive sweeps, retained after removing the power supply, and reprogrammed back to the initial high resistance state through a negatively-biased voltage sweeping exceeding –2.3 V (erase or RESET process). The OFF state of the sandwiched structures can be read and re-programmed to the ON state again in the subsequent positive sweeps, thus completing the bipolar "write-read-erase-read-rewrite" cycle for a non-volatile random access memory device. For this forming-free device, the initial state resistance is exactly the same as for that of the HRS after RESET. The operation cycles can be repeated with fairly good accuracy, and both the set and reset voltages are distributed uniformly with only minor (±4.3%) variation (Figure 2b). It was reported that the electrical stress might have an effect on the inherent electrical relaxation of the oxide materials and cause fluctuation of the electronic transport properties.[18] To explore the endurance properties of the devices, pulse operation with SET/RESET voltgaes of 3.0 V/–2.5 V and triggering period of 20 ns was executed for 5×10^7 cycles. Both the high and low resistance states (read at –0.1 V) are programmable, accessible and stable in these switching cycles, and they can be readily retained with a moderate HRS/LRS resistance (R_{OFF}/R_{ON}) ratio of 45 for at least 10^6 s (Figure 2c and Supporting Information, Figure S3). Simple extrapolation indicates that the retention of the bistable resistance states can be extended to more than 10 years with only a 17.6% decrease of the HRS/LRS resistance ratio. It is also believed that the

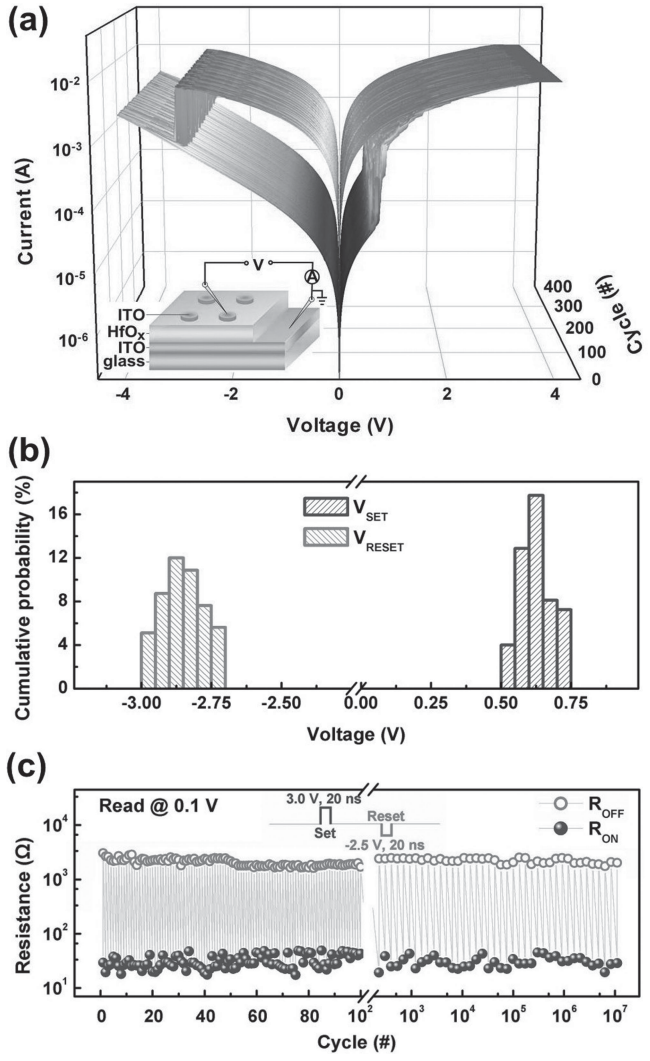

Figure 2. a) Current–voltage (*I–V*) characteristics of the ITO/HfO_x/ITO structure over 400 consecutive cycles. Inset shows the schematic illustration of the sandwich- structured device. b) Statistical distribution/cumulative probability of the set and rest voltages for the ITO/HfO_x/ITO switching structure. c) Room-temperature endurance characteristics of the switching device read at –0.1 V for both the high and low resistance states.

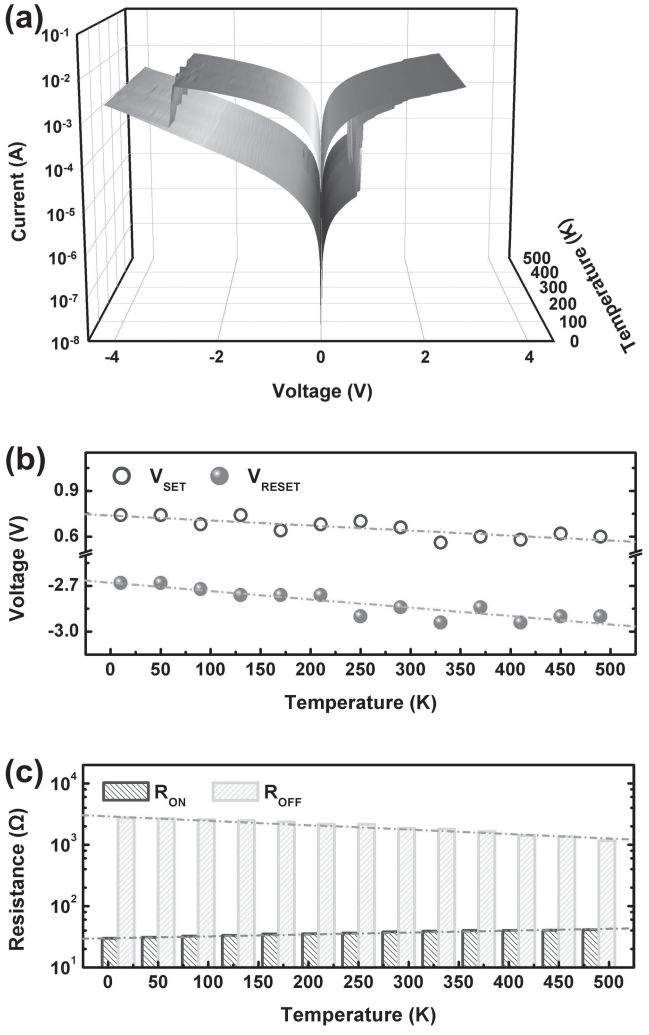

Figure 3. a) Electrical performance of the ITO/HfO_x/ITO switching structure at different temperatures. b) Evolution of the set and reset voltages as a function of the temperature. c) Endurance characteristic of temperatures read at –0.1 V in the high and low resistance states.

switching time of the present device is shorter than the width (20 ns) of the applied voltages.

The electrical performance of the ITO/HfO_x/ITO structure was also characterized at different temperatures to evaluate its capability of resisting the possible thermal shock when working under extreme environmental conditions. As shown in **Figure 3**a, the forming-free bipolar resistive switching phenomena are well maintained over the working temperature range of 10 K to 490 K. Starting from the room temperature where the SET and RESET voltages are 0.5 V and –2.3 V, respectively, neither does increasing nor decreasing the working temperature affect the programming field significantly. However, the SET and RESET voltages do slightly decrease as the working temperature increase, suggesting that the write and erase processes are activation energy-controlled procedures (Figure 3b).[19] The switching cycles almost follow the same trace, albeit the ON and OFF state resistances of the all-oxide device changes slightly (Figure 3c). As the working temperature increases from 10 K to 490 K, the ON state resistance increases from ≈30 Ω to 40 Ω accordingly. Such ON state resistance-temperature relationship is characteristics of a metallic conductor, and is discussed in the supporting information.[20] On the other hand, the increase in working temperature leads to decrease of the OFF state resistance from ≈3000 Ω to 1100 Ω, which correspond to the characteristic transport properties of a semiconductor.[21] Consequently, a slightly decreased R_{OFF}/R_{ON} ratio, which is still adequate to be used to identify the two states without severe misreading issue by today's state-of-the-art CMOS circuits, is observed during the device heating process.[9] Nonetheless, the working temperature of the present all-oxide device well covers that of the near-earth space. For instance, the sun-facing side of the moon is around 400 K while the shadow side is 40 K.[22] And the hafnium oxide devices demonstrate

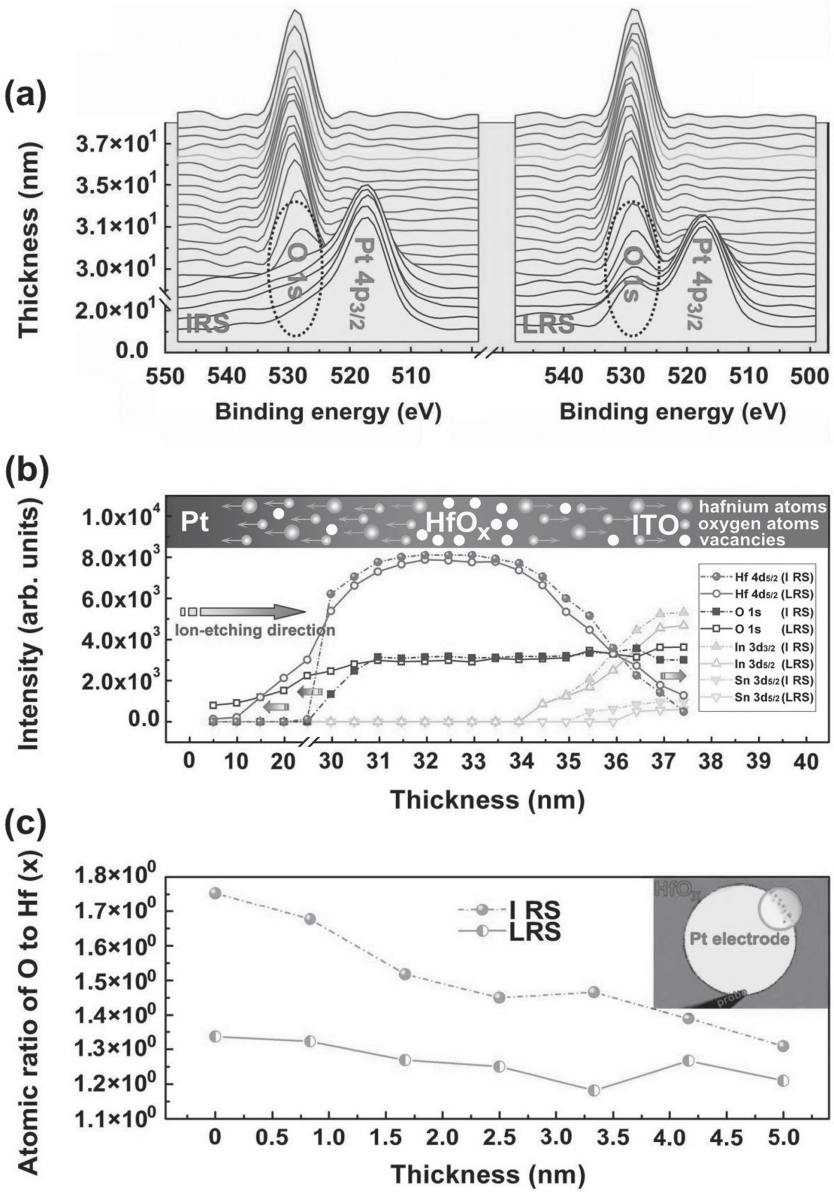

Figure 4. a) X-ray photoelectron spectroscopic (XPS) depth-profile of the Pt/HfO_x/ITO structure in the initial (upper) and low resistance (lower) states. b,c) The distribution of the constituent elements and the O:Hf ratio of the Pt/HfO_x/ITO structure in the initial and low resistance states, respectively. Inset of (c) shows the optical microscopic image of the Pt circular electrode after 10 consecutive switching cycles showing the minor degradation of the electrode edges.

great resistance to the proton and γ-ray irradiations.[23] Therefore, the thermally-stable resistive switching phenomena of the all-oxide device promise its great potential for outer-space data storage applications.

The formation and rupture of localized filamentary conduction path associated with the reduction-oxidation reaction of defects present in the oxide are widely accepted for the explanation of bipolar resistive switching in crystalline samples.[3b,24] Such valence-change based switching mechanism is usually driven by the drift of oxygen anions (O^{2-}) across the oxide layer towards the electrodes.[25] Leaving vacancies behind, the formation-rupture-regeneration of oxygen deficient conductive filaments can switch the oxide layer between low and high resistance states reprogrammablly.[26] In this mechanism, an initial process which requires a relative high voltage to form the conductive filaments along grain boundaries is usually necessary, though such a forming process is undesirable.[27] Severe constraints for circuit design, arising from the large discrepancy in the forming and subsequent setting voltages, as well as the substantial device degradation that leads to cycle-to-cycle and device-to-device variation under high electric field and limits the endurance performance of the memory device, hinders the commercialization of oxide based RRAMs.[28] In the present study, both polycrystalline and amorphous layers are present in the ITO/HfO_x/ITO devices. With the local deviation from ideal stoichiometry of the polycrystalline film, the electrically active defects lead to a forming-free bipolar resistive switching of the all-oxide devices. In addition, the low thermal budget requirement for integrating the RRAM device into the CMOS circuit delivers the mixed-structure hafnium oxide significant advantages over other crystalline samples.[29]

To gain insights into the conduction mechanism that gives rise to the stable and anti-thermal shock resistive switching behavior of the HfO_x-based devices, chemical composition of the storage layer has been investigated by X-ray photoelectron spectroscopic (XPS) depth-profiling analysis of the Pt/HfO_x/ITO cells in their respective initial resistance state (IRS) and low resistance state (**Figure 4** and Supporting Information, Figure S4). Here, to avoid the introduction of extra atoms from the TCO electrodes into the HfO_x film upon argon-ion etching treatment, inert platinum top electrode was used instead. With the present switching cells where transparent conductive oxide or noble metal was used as electrodes, the possibility of active electrode-metal diffusion can be excluded definitely.[30,31] As shown in the XPS depth-profiling spectra of the Pt/HfO_x/ITO cell in its initial resistance state, the oxygen 1s and hafnium $4p_{3/2}$ signals starts to be detected after the first five etching treatments, indicating that the Pt/HfO_x interface is located at ≈25 nm from the upper surface of the top electrode (Figure 4a). Similarly, the HfO_x/ITO interface can be located at the position next to where the seventh spectrum from the last, without any indium $3d_{3/2}$ signal, is received (Figure S4, Supporting Information). Ion-etching treatment can easily force the upper-layer atoms into their underlying substance, thus platinum and hafnium were detected in the hafnium oxide and ITO electrode layers, respectively.

In the O 1s core-level XPS spectra of the as-sputtered hafnium oxide film, both lattice oxygen species corresponding to

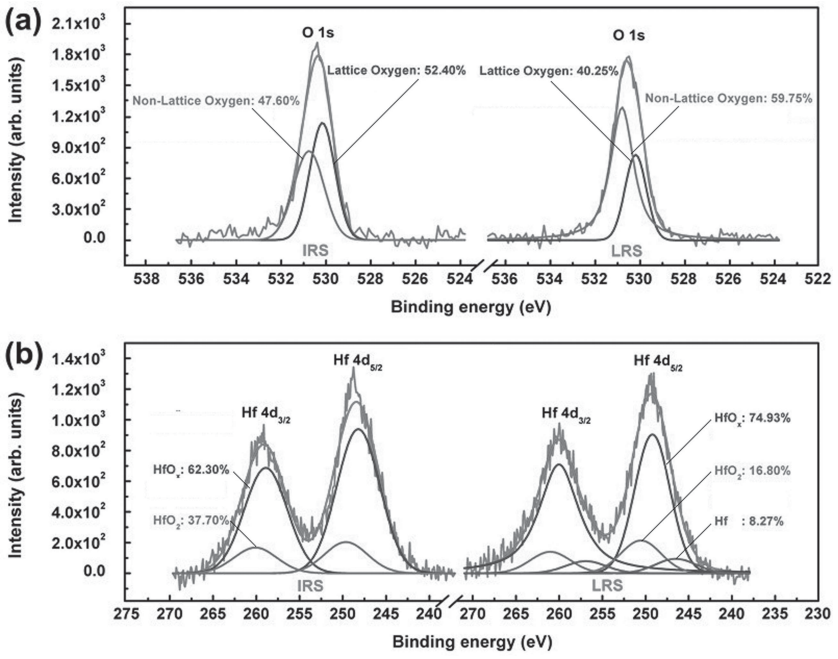

Figure 5. a) O 1s and b) Hf 4d core-level X-ray photoelectron spectra (XPS) of the ultrathin hafnium oxide film in the initial and low resistance states.

the O-Hf bonding and the non-lattice oxygen anions (O^{2-}) are revealed with the binding energies of 530.15 eV and 530.75 eV, respectively (**Figure 5**a). Upon being subject to the electric fields, the non-lattice oxygen anions as well as the hafnium cations in the oxide layer can migrate towards the electrodes (Figure S4, Supporting Information). As a result, the oxygen and hafnium content decreases in the switching thin film, while increases spontaneously in the electrode layers (Figure 4b). Quantitative analysis shows that oxygen anions drift faster than the hafnium cations (Figure 4c and Supporting Information, Figure S5). After transition to the low resistance state, the O:Hf atomic ratio of the bulk film (for instance, 2.5 nm from the top) decreases from 1.45 to 1.25, which is much lower than that of the Pt/HfO_x interface (1.33). Therefore, the migration of oxygen ions is suggested to dominate the formation and rupture of conductive filaments across the hafnium oxide thin films. According to the experimental procedure where the deposition atmosphere with an O_2/Ar ratio of 1:5 was used to fabricate the oxygen deficient HfO_x layer, numerous amounts of oxygen vacancies (or movable non-lattice oxygen anions) pre-exist in the oxide film. Under electric field, the concentration of charged oxygen vacancies can exceed the percolation threshold easily, and induces the insulating-to-conductive transition of the oxide layer without a forming stage.[28] As the HfO_x layer is practically thin, a small setting voltage (0.5 V) is sufficient to switch the device ON and OFF. After switching to the low resistance state, the non-lattice oxygen species also increase from ≈47.60% to ≈59.75%, and become dominant across the HfO_x film (Figure 5b). Increase in the device temperature may assist the generation of oxygen vacancies in the SET process, or promote the migration of oxygen anions back from the electrode to the oxide layer, thus both the set and reset voltages decrease correspondingly (Figure 3b).[4f] Moreover, the migration, electrochemical oxidation and evaporation of oxygen species is further confirmed by the minor degradation of the top platinum electrode, where the edge of the circular electrode becomes bubbled (oxidized) and less smooth after 10 electrical switching cycles (inset of Figure 4c and Supporting Information, Figure S5).[32]

Nevertheless, the core-level Hf 4d XPS spectra provide essential information for identifying the chemical nature of the conductive filaments in the ultrathin film of hafnium oxide (Figure 5).[4f,32a,33] In the initial resistance state, the presence of the Hf $4d_{5/2}$ and Hf $4d_{3/2}$ species with the binding energies of 248.22 eV and 258.94 eV corresponds to the predominant HfO_x component where x is less than 2, while the minor high-binding energy Hf $4d_{5/2}$ and Hf $4d_{3/2}$ species at 249.58 eV and 260.09 eV are associated with the HfO_2 components. The relatively weak intensity of the HfO_2 components is in accordance with the fact that during RF magnetron sputtering deposition, low-pressure atmosphere with a small O_2/Ar ratio of 1:5 were maintained in the chamber, resulting in the low oxidative state of the metal ion in the ultrathin film. With the presentative x number of 1.45 (2.5 nm from the Pt/HfO_x interface) and the relative strength of the two hafnium oxide components, which is calculated from the corresponding XPS peak areas, the pristine HfO_x thin film demonstrates a chemical composition of 56.30% of $HfO_{1.24}$ and 37.70% of HfO_2. As a net effect of the co-existence of the two hafnium oxide constituents, the as-sputtered HfO_x thin film carries an oxygen vacancy concentration of ≈27.5%. Upon switching the hafnium oxide layer to the low resistance state, the Hf 4d core-level XPS spectrum exhibits a non-negligible appearance of the new Hf $4d_{5/2}$ and Hf $4d_{3/2}$ species at 248.29 eV and 259.12 eV. The low-binding energy Hf species can be attributed to the electrochemically-reduced metallic hafnium atoms, and are further correlated by the linear temperature dependence of the LRS metallic resistance with the formula of $R(T) = R_0[1 - \alpha(T - T_0)]$, where R_0 is the resistance at temperature T_0, and α is the temperature coefficient of resistance (Figure S6, Supporting Information). The calculated α of the LRS hafnium oxide film is 4.0×10^{-3} K^{-1} in the temperature range of 273 K to 300 K, similar to the reported value of 3.9×10^{-3} K^{-1} for high-purity hafnium nanowire.[34] Therefore, the metallic hafnium-rich nature of the conductive filaments that cause the electrical switching of the device resistance to a much lower level is confirmed.[35] The LRS hafnium oxide film has a chemical composition of Hf: $HfO_{1.22}$: HfO_2 = 1: 9.06: 2.03, suggesting that 8.27% hafnium atoms can participate in the formation of the metallic conductive filaments in the HfO_x switching layer. It is noteworthy that the stoichiometry number of the dominant hafnia species ($HfO_{1.24\text{-}1.22}$) remains almost constant, while the relative concentration increases from 56.30% to 74.94%. Thus the conductive filaments are mainly

from the electrochemical metallization of the quadrivalent hafnium cations of the stoichiometric HfO_2 species.

As discussed previously, the conductive filaments that are responsible for the resistive switching in oxide materials are usually energetically-favorably located at grain boundaries. Associated with the abundant numbers of crystalline and chemical defects of dangling bonds, such filaments can result in severe leakage in polycrystalline sample and consequently permanent breakdown of the switching devices.[36] In the present study, the polycrystalline structure of the middle HfO_x layer also leads to a large OFF state current. On the other hand, as the polycrystalline hafnium oxide layer is buried under amorphous interfacial layers, less leaking paths associated with the grain boundaries are exposed directly to the ITO electrodes. Therefore, significant improvement in the retention and endurance performance of the memories are accounted. As the conductive filaments are metallic, it is natural to observe a positive dependence of the LRS resistance on the device temperature, whereas the space-charge-limited-current (SCLC) controlled HRS resistance decreases as temperature increases (see Supporting Information, Figures S6,S7).

The current-voltage characteristics of the bistable resistance states were curve-fitted with appropriate charge transport models and re-plotted with double logarithmic scale in **Figure 6**a and 6b, respectively. In insulating or semiconducting materials, the carrier concentration is strongly-related to the energy band gaps. The wide band gap (≈6 eV) of the mixed-phase hafnium oxide leads to a lower concentration of the thermally-generated charge carriers (charged oxygen vacancies) and consequently the insulating nature of the ultrathin films. XPS data indicates that the as-sputtered HfO_x film carries an x value of 1.4–1.8 in close proximity to that of the chemically-stoichiometric HfO_2 while the electrically-switched hafnium oxide has a much smaller x number of 1.2–1.3. Therefore, an average oxygen vacancy concentration of 30% and 40% can be derived for the as-sputtered and electrically-switched HfO_x films, respectively. Though the presence of small amount of oxygen vacancies offers a means of low-energy charge transport paths in the as-sputtered thin film, the limited density of the non-stoichiometric defect states present in the band gap of the hafnium oxide is less efficient for the thermal generation of charge carriers. As a result, the pristine ITO/HfO_x/ITO structure is in its initial high resistance state and Ohmic conduction was observed in the low voltage region.

With electric-field increased, an increased oxygen vacancy content can be expected. For instance, when the x value is 1.32, the larger density of defect states is more favorable for the generation of carriers. As the number of injected carriers becomes comparable with that of thermal free carriers, carrier conduction becomes determined mainly by the shallow traps. The carriers trapped near the electrode form a space charge layer, which limited further electrode injection. Therefore, the electronic transport deviates substantially from Ohmic conduction, giving rise to a square-law dependent behavior. The resistance of the HRS hafnium oxide decreases as temperature increases (Figure 6c), and is consistent with the temperature-dependent thermal generation of charge carrier in semiconductor materials. Once the ITO/HfO_x/ITO structure has been set to the low resistance state, the large amount of oxygen vacancy (38%) and defects states benefit both the generation and transport of charge carriers. As a result, the LRS conduction regains the Ohmic (Figure 6b) and metallic (Figure 6d) nature, where the resistance of the sandwiched structure increases with the rising of sampling temperature.

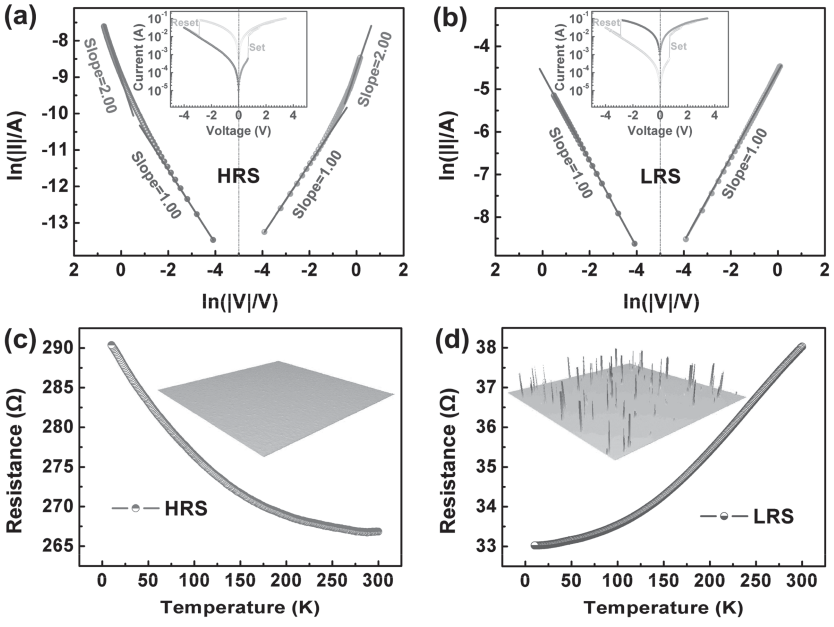

Figure 6. Experimental and fitted current–voltage (I–V) curves in log-log scale for the a) initial and b) low resistance states. Insert shows the corresponding I–V curve in line-log scale. Temperature dependence of the resistance and conductive-atomic force microscopic (C-AFM) mapping of the ultrathin hafnium oxide film in the c) initial and d) low resistance states.

In comparison with that of the hafnium oxide in its high resistance state, the conductive atomic force microscopic (C-AFM) mapping of the electrically-switched HfO_x/ITO structure suggests that filamentary conduction is responsible for the low resistance state in the HfO_x thin film (inset of Figure 6c,d). Device area-dependent behavior of the LRS filamentary conduction was also confirmed as shown in **Figure 7**. In the HRS, the conduction over the entire device ares is uniform (inset of Figure 6c), therefore the current flowing across the device (or the device resistance) shows area-dependence and is propotional (or reversibly propotional) to the device area. When switched to the LRS, filamentary conduction becomes dominent. As shown in the inset of Figure 6d, current flows preferentially from the localized conductive filaments. As the formation, rupture and regeneration of the conductive filaments are random, the current flowing across the device (or the device resistance) is consequently area-independence. Moreover, the high melting temperatures of the metallic hafnium and hafnium oxide, which are 2233 °C and 2800 °C, respectively, are the

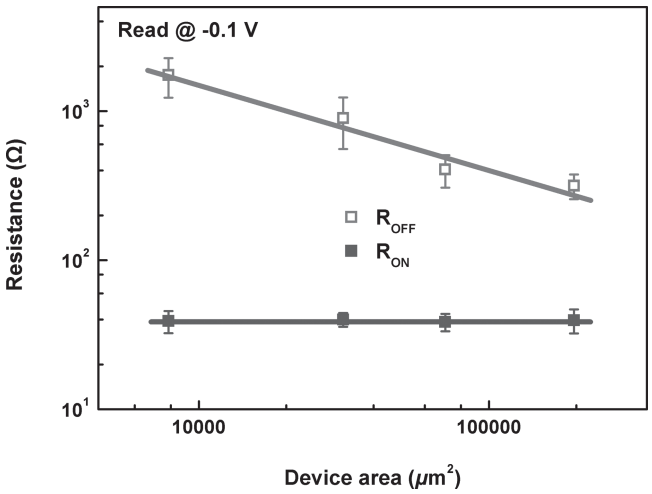

Figure 7. Device-area dependence of the resistance for the ITO/HfO_x/ITO switching structure in its high and low resistance states.

physical origin of the anti-thermal shock capability of the all-oxide T-RRAM devices.[15,37]

3. Conclusion

In this work, fully transparent resistive random access memory devices based on an ITO/HfO_x/ITO sandwiched structure were fabricated using RF magnetron sputtering technique. The all-oxide device demonstrates good transparency over the visible spectrum of the solar irradiation, which can be further enhanced by using more transparent TCO electrodes. Without an initial electro-forming process, the T-RRAM devices show asymmetric bipolar resistive switching behavior with large R_{OFF}/R_{ON} ratio of 45, excellent endurance of over 400 operating cycles, extrapolated retention ability approaching 10 years and wide working temperature range of 10 K to 490 K. The bistable electrical switching is ascribed to the electric field-induced migration of oxygen anions and the simultaneous formation of metallic hafnium-rich conductive filaments. Together with the ultrathin and optically-transparent characteristics, as well as the stable, and anti-thermal shock electrical switching properties of the ITO/HfO_x/ITO sandwich structure, the present mixed-structure HfO_x based all-oxide device renders promising memory capability and optical transmittance for T-RRAM applications.

4. Experimental Section

Device Fabrication: High purity HfO_x ceramic (99.995%) with a 2 inch-diameter and 3 mm-thickness was used as the sputtering target. The 5 nm-HfO_x film was deposited on a commercial ITO-coated glass substrate by RF magnetron sputtering technique (JGP450 system, SKY Technology CAS) at room temperature with a base pressure of lower than 1.2×10^{-4} Pa. High purity Ar (99.999%) and O_2 (99.999%) with the O_2/Ar ratio of 1:5 were introduced into the chamber during the deposition. The RF power and working pressure were fixed at 60 W and 1 Pa during the sputtering process, respectively. The 100-nm-thick ITO top electrodes with diameter of 100 μm were deposited by sputtering an ITO target using pulsed laser deposition (PLD) technique (PLD300 system from SKY Technology CAS, equipped with COMPEXPRO 205 excimer laser generator from Lambda Physik) and patterned through a metal shadow mask.

Characterization: The crystalline structure of the as-deposited HfO_x films was investigated by grazing-incidence X-ray diffraction technique (GIXRD, Bruker AXS, D8 Discover) using Cu-K_α radiation. The incidence angle of X-ray beam was fixed at 1° and the measurements were recorded with a step of 0.05° in the range of 10° to 70°. The thickness of the films was determined using field-emission scanning electron microscopy (FESEM, Hitachi, S-4800) with 15 kV accelerating voltage. The optical transmission spectra were recorded using UV–Vis–NIR Spectrometer (Perkin Elmer, Lambda 950) in the wavelength range of 200 nm to 2000 nm. The current-voltage (*I–V*) characteristics of the ITO/HfO_x/ITO structures were measured on a Lakeshore probe station equipped with a precision semiconductor parameter analyzer (Keithley 4200) in dc sweep mode. During the *I–V* measurements, ITO bottom electrodes were always grounded and the biased-voltages were applied to the top electrode. The temperature dependence of the resistance (R-T) for the ITO/HfO_x/ITO devices was examined on a physical property measurement system (PPMS, Quantum Design, Model-9) using a conventional two-probe method. The patterned-ITO top electrodes were inter-connected with thin platinum (Pt) wires using highly conductive silver glue (EPO-TEK H20E from Epoxy Technology, Inc., volume resistivity @ 23° ≤ 0.0004 Ohm-cm) followed by welding of the Pt wires onto the PPMS sample stage. During R-T measurement, a constant-current mode with an excitation current of 50 μA was used. Scanning probe microscopy (Veeco, Dimension 3100V) equipped with a conducting cantilever coated with Pt/Ir was employed for C-AFM measurements of the HfO_x/ITO structures, where the AFM tip was always grounded while the biased-voltages were applied to the ITO layer.

X-Ray Photoelectron Spectroscopy: In order to investigate the film composition and oxidative states of the hafnium species in the initial and low resistance states, depth-profiling of the Pt/HfO_x/ITO structure was performed using ion-etching treatment during X-ray photoelectron spectroscopic (XPS, SHIMADZU, AXIS ULTRA DLD) measurements. A monochromatic Al-Kα X-ray source (1486.6 eV photons) was used at a constant dwell time of 100 ms. A pass energy of 80 eV or 40 eV was employed for the wide and core-level spectra scan, respectively. The X-ray source was run at a reduced power of 150 W (15 kV and 10 mA). The pressure in the analysis chamber was maintained at 10^{-8} Torr or lower during each measurement. The core-level signals were recorded at a photoelectron take-off angle (α, measured with respect to the sample surface) of 90°. All binding energies (BEs) were referenced to the C 1s hydrocarbon peak at 284.6 eV. In curve fitting, the line width (full width at half-maximum, or FWHM) for the Gaussian peaks was maintained constant for all components in a particular spectrum. Surface elemental stoichiometries were determined from XPS spectral area ratios and were reliable within ±5%. The elemental sensitivity factors were calibrated using stable binary compounds of well established stoichiometries. Each ion-etching operation unveiled a brand-new surface and the XPS spectra provided the means of analyzing the composition of these surfaces. Background correction and peak fit features were performed to the data using CASA XPS software.

Supporting Information

Supporting Information is available from the Wiley Online Library or from the author.

Acknowledgements

This work was supported by the State Key Research Program of China (973 Program, 2009CB930803, 2012CB933004), Chinese Academy of Sciences (CAS), National Natural Science Foundation

of China (51172250, 51303194, 61328402, 61306152), Zhejiang and Ningbo Natural Science Foundations (2013A610031), and Science and Technology Innovative Research Team of Ningbo Municipality (2009B21005, 2011B82004). The authors also would like to thank Dr. Katlakunta Sadhana for polishing the manuscript.

Received: September 23, 2013
Revised: July 10, 2013
Published online: November 27, 2013

[1] a) G. Thomas, *Nature* **1997**, *389*, 907–908; b) J. F. Wager, *Science* **2003**, *300*, 1245–1246; c) L. Wang, M. H. Yoon, G. Lu, Y. Yang, A. Facchetti, T. J. Marks, Tobin, *Nat. Mater.*, **2006**, *5*, 893–900.

[2] a) C. Bechinger, S. Ferrer, A. Zaban, J. Sprague, B. A. Gregg, *Nature* **1996**, *383*, 608–610; b) D. Fattal, Z. Peng, T. Tho, S. Vo, M. Fiorentino, J. Brug, R. G. Beausoleil, *Nature* **2013**, *495*, 348–351.

[3] a) R. Waser, M. Aono, *Nat. Mater.* **2007**, *6*, 833–840; b) A. Sawa, *Mater. Today* **2008**, 28–36.

[4] a) K. C. Liu, W. H. Tzeng, K. M. Chang, Y. C. Chan, C. C. Kuo, *Microelectron. Eng.* **2011**, *88*, 1586–1589; b) Y. Meng, P. J. Zhang, Z. Y. Liu, Z. L. Liao, X. Y. Pan, X. J. Liang, H. W. Zhao, D. M. Chen, *Chin. Phys. B* **2010**, *19*, 037304; c) Y. S. Wang, *Phys. Status Solidi A* **2012**, *209*, 364–368; d) K. Zheng, X. W. Sun, J. L. Zhao, Y. Wang, H. Y. Yu, H. V. Demir, K. L. Teo, *IEEE Elec. Dev. Lett.* **2011**, *32*, 797–799; e) L. Shi, D. S. Shang, J. R. Sun, B. G. Shen, *Appl. Phys. Express* **2009**, *2*, 101602; f) M. C. Chen, T. C. Chang, S. Y. Huang, S. C. Chen, C. W. Hu, C. T. Tsai, S. M. Sze, *Electrochem. Solid-State Lett.* **2010**, *13*, H191–H193.

[5] a) A. Facchetti, T. J. Marks, *Transparent Electronics: From Synthesis to Applications*, **2010**. John Wiley & Sons Ltd, West Sussex, UK 2010; b) H. Hosono, *Thin Solid Films* **2007**, *515*, 6000–6014.

[6] G. S. Herman, J. S. Rajachidambaram, M. S. Rajachidambaram, S. Y. Han, C. H. Chang, S. Murali, J. F. Conley Jr., *IEEE Photonics Conf.* **2011**, 555–563.

[7] a) K. Kinoshita, T. Okutani, H. Tanaka, T. Hinoki, H. Agura, K. Yazawa, K. Ohmi, S. Kishida, *Solid-State Electron.* **2011**, *58*, 48–53; b) S. Jung, J. Kong, S. Song, K. Lee, T. Lee, H. Hwang, S. Jeon, *Microenectron. Eng.* **2011**, *88*, 1143–1147; c) H. Y. Jeong, J. Y. Lee, S. Y. Choi, *Adv. Funct. Mater.* **2010**, *20*, 3912–3917.

[8] H. D. Kim, H. M. An, Y. Seo, T. G. Kim, *IEEE Electron. Dev. Lett.* **2011**, *32*, 1125–1127.

[9] D. S. Jeong, R. Thomas, R. S. Katiyar, J. F. Scott, H. Kohlstedt, A. Petraru, C. S. Hwang, *Rep. Prog. Phys.* **2012**, *75*, 076502.

[10] D. G. Schlom, J. H. Haeni, *MRS Bull.* **2002**, *27*, 198–204.

[11] a) M. Balog, M. Schieber, M. Michman, S. Patai, *Thin Solid Films* **1997**, *41*, 247–259; b) S. G. Lim, S. Kriventsov, T. N. Jackson, J. H. Haeni, D. G. Schlom, A. M. Balbashov, R. Uecker, P. Reich, J. L. Freeouf, G. Lucovsky, *J. Appl. Phys.* **2002**, *91*, 4500–4505.

[12] a) S. Lee, D. L. Kwong, *Jpn. J. Appl. Phys.* **2003**, *42*, 7256–7258; b) J. Robertson, *Rep. Prog. Phys.* **2006**, *69*, 327–396.

[13] a) M. Alvisi, M. Di Giulio, S. G. Marrone, M. R. Perrone, M. L. Protopapa, A. Valentini, L. Vasanelli, *Thin Solid Films* **2000**, *358*, 250–258; b) M. Gilo, N. Croitoru, *Thin Solid Films* **1999**, *350*, 203–208.

[14] P. Rauwel, E. rauwel, C. Persson, M. F. Sunding, A. Galeckas, *J. Appl. Phys.* **2012**, *112*, 104107.

[15] a) X. Y. Zhao, D. Vanderbilt, *Phys. Rev. B* **2002**, *65*, 233106; b) S. Capone, G. Leo, R. Rella, P. Siciliano, L. Vasanelli, M. Alvisi, L. Mirenghi, A. Rizzo, *J. Vac. Sci. Technol. A* **1998**, *16*, 3564–3568.

[16] Y. K. Schuller, *Phys. Rev. B* **1980**, *24*, 1597–1600.

[17] H. Kim, C. M. Gilmore, A. Piqué, J. S. Horwitz, H. Mattoussi, H. Murata, Z. H. Kafafi, D. B. Chrisey, *J. Appl. Phys.* **1999**, *86*, 6451–6461.

[18] a) V. Provenzano, L. P. Boesch, V. Volterra, C. T. Moynihan, P. B. Macedo, *J. Am. Ceram. Soc.* **1972**, *55*, 492–496; b) J. B. Wachtman Jr., *Phys. Rev.* **1963**, *131*, 517–527.

[19] C. Walczyk, D. Walczyk, T. Schroeder, T. Bertaud, M. Sowińska, M. Lukosius, M. Fraschke, D. Wolansky, B. Tillack, E. Miranda, C. Wenger, *IEEE Trans. Electron. Dev.* **2011**, *58*, 3124–3131.

[20] N. F. Mott, *Can. J. Phys.* **1956**, *34*, 1356–1368.

[21] G. Grundmann, *The Physics of Semiconductors: An Introduction including Nanophysics and Applications, 2nd ed.*, Springer-Verlag Berlin, Heidelberg **2010**.

[22] V. D. Krotikov, V. S. Troitskiĭ, *Sov. Phys. Usp.* **1964**, *6*, 841–871.

[23] a) Y. Wang, H. Lv, W. Wang, Q. Liu, S. Long, Q. Wang, Z. Huo, S. Zhang, Y. Li, Q. Zuo, W. Lian, J. Yang, M. Liu, *IEEE, Electron Device Lett.* **2010**, *31*, 1470–1472; b) B. Butcher, X. He, M. Huang, Y. Wang, Q. Liu, H. Lv, M. Liu, W. Wang, *Nanotechnology*, **2010**, *21*, 475206.

[24] a) Y. E. Syu, T. C. Chang, T. M. Tsai, Y. C. Hung, K. C. Chang, M. J. Tsai, M. J. Kao, S. M. Sze, *IEEE Electron Device Lett.* **2011**, *32*, 545–547; b) Y. E. Syu, T. C. Chang, J. H. Lou, T. M. Tsai, K. C. Chang, M. J. Tsai, Y. L. Wang, M. Liu, Simon M. Sze, *Appl. Phys. Lett.* **2013**, *102*, 172903.

[25] J. J. Yang, F. Miao, M. D. Pickett, D. A. A. Ohlberg, D. R. Stewart, C. N. Lau, R. S. Williams, *Nanotechnology* **2009**, *20*, 215201.

[26] T. Nagata, M. Haemori, Y. Yamashita, Y. Iwashita, H. Yoshikawa, K. Kobayashi, T. Chikyow, *Appl. Phys. Lett.* **2010**, *97*, 082902.

[27] X. Wu, Z. Fang, K. Li, M. Bosman, N. Raghavan, X. Li, H. Y. Yu, N. Singh, G. Q. Lo, X. X. Zhang, K. L. Pey, *Appl. Phys. Lett.* **2011**, *99*, 133504.

[28] Y. S. Chen, H. Y. Lee, P. S. Chen, T. Y. Wu, C. C. Wang, P. J. Tzeng, F. Chen, M. J. Tsai, C. Lien, *IEEE Electron. Dev. Lett.* **2010**, *31*, 1473–1475.

[29] S. Clima, Y. Y. Chen, R. Dergraeve, M. Mees, K. Sankaran, B. Govoreau, M. Jurczak, S. De Gendt, G. Pourtois, *Appl. Phys. Lett.* **2012**, *100*, 133102.

[30] M. Y. Chan, T. Zhang, V. Ho, P. S. Lee, *Microelectron. Eng.* **2008**, *85*, 2420–2424.

[31] a) X. J. Zhu, W. J. Su, Y. W. Liu, B. Hu, L. Pan, W. Lu, J. D. Zhang, R. W. Li, *Adv. Mater.* **2012**, *24*, 3941–3946; b) R. Waser, R. Dittmann, G. Staikov, K. Szot, *Adv. Mater.* **2009**, *21*, 2632–2633.

[32] a) T. Nagata, M. Haemori, Y. Yamashita, H. Yoshikawa, Y. Iwashita, K. Kobayashi, T. Chikyow, *Appl. Phys. Lett.* **2012**, *99*, 223517; b) A. J. Bard, L. R. Faulkner, *Electrochemical Methods. Fundamentals and Applications*, 2nd ed, Wiley-New York 2001.

[33] J. Chastain, *Handbook of X-ray Photoelectron Spectroscopy*, Perkin-Elmer Corp., Physical Electronics Division, Eden Prairie, MN, 1992.

[34] R. C. Weast, M. J. Astle, *CRC Handbook of Chemistry and Physics: A Ready-Reference Book of Chemical and Physical Data*, CRC Press, Boca Raton, FL 1980.

[35] a) J. H. Mooij, *Phys. Status Solidi A* **1973**, *17*, 521–530; b) J. H. Schemel, *ASTM Manual on Zirconium and Hafnium (Vol 639)*, ASTM International, UK **1977**.

[36] a) P. Calka, E. Martinez, D. Lafond, H. Dansas, S. Tirano, V. Jousseaume, F. Bertin, C. Guedj, *Microelectron. Eng.* **2011**, *88*, 1140–1142; b) K. M. Chang, W. H. Tzeng, K. C. Liu, Y. C. Chan, C. C. Kuo, *Microelectron. Reliab.* **2010**, *50*, 1931–1934.

[37] D. K. Deardorff, E. T. Hayes, *J. Metal* **1956**, *8*, 509–511.